



# LGM glaciers in the SE Mediterranean? First evidence from glacial landforms and $^{36}\text{Cl}$ dating on Mount Lebanon



A. Moulin <sup>a, f</sup>, L. Benedetti <sup>a, \*</sup>, L. Vidal <sup>a</sup>, J. Hage-Hassan <sup>a</sup>, A. Elias <sup>b</sup>, J. Van der Woerd <sup>c</sup>, I. Schimmelpfennig <sup>a</sup>, M. Daëron <sup>d</sup>, P. Tapponnier <sup>e</sup>

<sup>a</sup> Aix Marseille Univ, CNRS, IRD, INRAE, Coll France, CEREGE, Aix-en-Provence, France

<sup>b</sup> Lebanese University, Faculty of Engineering I, Ras Maska, Lebanon

<sup>c</sup> Institut de Physique du Globe de Strasbourg, UMR 7516, CNRS, Université de Strasbourg, France

<sup>d</sup> Laboratoire des Sciences du Climat et de l'Environnement, LSCE/IPSL, CEA-CNRS-UVSQ, Université Paris-Saclay, Gif-sur-Yvette, France

<sup>e</sup> Institute of Crustal Dynamics, China Earthquake Administration, China

<sup>f</sup> Physical Science and Engineering Division, King Abdullah University of Science and Technology, Thuwal, Saudi Arabia

## ARTICLE INFO

### Article history:

Received 24 November 2021

Received in revised form

27 March 2022

Accepted 29 March 2022

Available online 26 April 2022

Handling Editor: C. O'Coifagh

### Keywords:

Mount Lebanon

Glacial morphology

$^{36}\text{Cl}$ -dating

Levant paleoclimate

## ABSTRACT

The hydrological conditions during the Last Glacial Maximum in the Eastern Mediterranean have long been debated. In particular, very little is known about the development of high-altitude glaciers in this region. In the present study, morphological and sedimentological evidence, such as U-shape valleys, glacial cirques, and morainic ridges, are used to identify past glaciers on the western slopes of Mount Lebanon, which is by far the highest topography along the eastern Mediterranean coast (3088 m a.s.l.). The geometry of three paleo-glaciers is reconstructed: one 8-km-long glacial tongue stretching from the highest peak down to an elevation of about 2000 m a.s.l., and two small glacial cirques located at about 2300 m a.s.l. The age of maximum glacier advance is constrained from a 10-m-deep  $^{36}\text{Cl}$  depth-profile within the diamicton of one terminal moraine, and yields an early LGM timing (between  $25.4 \pm 3.1$  ka and  $31.2 \pm 4.5$  ka), which agrees with the chronology of the last maximum glacier extension in the Eastern Mediterranean. The three glaciers together form a consistent group, compatible with an Equilibrium Line Altitude (ELA) at 2400 m estimated using the Accumulation Area Ratio method. A degree-day model is further used to infer the temperature and precipitation conditions required to depress the LGM ELA to 2400 m. Our results suggest that the observed glacier extent is compatible with early LGM paleo-temperature records of the area only under the condition of decreased precipitation relative to modern times. These findings thus support an early LGM climate of the Levant region that was drier than today.

© 2022 Elsevier Ltd. All rights reserved.

## 1. Introduction

The Last Glacial Maximum (LGM) corresponds to the last time interval in Earth's history, when the globally-integrated volume of ice sheets reached its maximum under the influence of external forcing (Mix et al., 2001). The timing of the LGM varies depending on the type of used geological record (e.g. between 26 and 19 ka from globally-averaged sea-level records (Clark et al., 2009) versus between 28 and 23 ka from atmospheric dust flux recorded in polar ice cores (Hughes and Gibbard, 2015)). In any case, the mode and

rate at which external forcing mechanisms are transmitted to Earth's surface and control local climates are neither homogeneous nor fully understood. Reconstructing the distribution of LGM climate parameters in space and time with sufficient resolution is thus essential to solve for the spatial variability of the LGM climate. Moreover, these reconstructions allow for investigation of the feedbacks involved in the transition from glacial to interglacial periods in areas located far away from polar regions, thus improving our understanding of modern climate dynamics, as well as our ability to forecast climate evolution. Local paleoclimate reconstructions are fundamental to disentangle how global forcing is modulated at regional/local scales, how local climates interact with each other, and thus permit to improve large-scale climatic models. The Mediterranean region is highly sensitive to global climate

\* Corresponding author.

E-mail address: [benedetti@cerge.fr](mailto:benedetti@cerge.fr) (L. Benedetti).

change. Paleoclimatic records indicate that the LGM in the Mediterranean was marked by a northwestward gradient of both the atmospheric temperature anomaly (relative to the present), reaching a maximum of  $-17^{\circ}\text{C}$  in the Alps (Wu et al., 2007) (pollen-data-based reconstructions), and the sea surface temperature anomalies (Mikolajewicz, 2011). Superimposed on these regional trends are glacial refugia, where the LGM climate was locally buffered, as indicated by the persistence of endemic species in climatic niches over geological times (e.g. Médail and Diadema, 2009; Petit et al., 2003), making the Mediterranean a hotspot of biodiversity.

Here, we study a new LGM climatic record from Mount Lebanon (coastal Levant, Eastern Mediterranean), a mountainous environment system (Dubertret, 1955; Sanlaville, 1977) where local responses to climate forcing are expected. The Levant region (Fig. 1b) is located in a transitional zone between the temperate Mediterranean climate to the North and the sub-tropical high-pressure zone to the South (Hajar et al., 2010; Develle et al., 2011). Its modern climate is typically Mediterranean, on which topographic and continental effects are superimposed locally due to the presence of high mountain ranges (Mt Lebanon 3088 m a.s.l., Figs. 1b and 2a). Paleotemperature reconstructions based on several proxies suggest a mean annual LGM temperature difference (relative to present) ranging between  $-6$  and  $-14^{\circ}\text{C}$  indicating a broad agreement for a regional glacial cooling (Affek et al., 2008; Almogi-Labin et al., 2009; Emeis et al., 2003; Essallami et al., 2007; McGarry et al., 2004; Wu et al., 2007). The main debate about the glacial climate of the Levant region deals with the question whether it was dry or wet (Develle et al., 2011; Miebach et al., 2019). Although paleohydrological records show pronounced changes associated with the last glacial stage across the whole region, there is a marked disparity in the spatial response between the central and southern Levant. In the central Levant, records from the Yammouneh paleolake in Lebanon indicate that the LGM was a period of reduced water balance of the lake (Develle et al., 2011; Gasse et al., 2015). In the southern Levant on the other hand, some 150 km further south in Israel (Fig. 1b), soil sequence stratigraphy was used by Gvirtzman and Wieder (2001) to infer wet LGM conditions. LGM lake highstands in the Lisan Dead Sea Basin have also long been attributed to increased precipitation (Stein et al., 2010; Torfstein et al., 2013a,b), although this latter interpretation has been recently questioned (Miebach et al., 2019; Stockhecke et al., 2016).

The present study focuses on glacial deposits, a type of continental record that can be more robustly interpreted in terms of temperature and precipitation, as the advances/retreats of glaciers respond quickly to changes in the local Equilibrium Line Altitude (=ELA) (Porter, 2000) and hence to the vertical structure of the atmosphere (Braithwaite, 2008). The ELA is the elevation where the annual mass balance of snow/ice is zero, and above which ice forms by accumulation of snow over years (Porter, 2000). The size of glaciers and their downward extent are therefore strongly regulated by the local temperature and precipitation (Blard et al., 2009; Hughes et al., 2010; Jomelli et al., 2009; Oerlemans, 2005; Protin et al., 2019; Rabatel et al., 2008), although secondary factors such as slope orientation, wind, avalanches, can also contribute significantly to the distribution of glaciers (Dahl and Nesje, 1992; Farinotti et al., 2020; Hewitt et al., 2011). Around the Mediterranean, large LGM glaciers concentrate along an ENE-WSW-trending line running from the Carpathian (Romania) to the Cantabrian (Spain) Mountains, and culminating in the Alpine ice sheet (LGM ELA between 1000 and 1500 m) (Fig. 1a). Based on erosional and depositional features, evidence of small LGM glaciers were also found locally in other unfavorable (more southern) circum-Mediterranean areas, where topographic highs exceeded the LGM ELA (i.e. in Morocco, Spain, Italy, Balkans, Greece, and Turkey)

(Kuhlemann et al., 2008; Hughes and Woodward, 2017) (Fig. 1a). All so far known LGM Mediterranean glaciers are located NW of a line connecting eastern Turkey to central Morocco (Allard et al., 2021; Allen et al., 2008; Ehlers and Gibbard, 2004; Hughes and Woodward, 2017; Kuhlemann et al., 2008) (Fig. 1a). The only known LGM glaciers south of latitude  $37^{\circ}\text{N}$  are located on the Atlantic seaboard, on the up-to-4000-m topography of the Atlas Mountains (Morocco; LGM ELA between 2400 and 3200 m) (Fig. 1a) (Hughes et al., 2020). It should be acknowledged however that the preservation of morainic deposits on Mount Lebanon and Mount Hermon (Lebanon) was reported by Messerli (1966). If confirmed, the existence of these glacial records at this latitude ( $34^{\circ}\text{N}$ ) of the Levant region would extend the southeastern limit of former Mediterranean glaciers by several hundreds of kilometers (Fig. 1a).

The basic strategy when reconstructing paleoclimate parameters from glacial deposits is to identify terminal moraines (i.e. the sedimentary formations left in front of a glacier when the latter starts retreating after a phase of equilibrium; Refsnider et al., 2008), to date them, and then to calculate the ELA required to allow the glacier advancing down to that terminal moraine (Blard et al., 2009; Protin et al., 2019). The ELA is essentially a bivariate system, which in most cases, highly depends on the temperature, and in a lesser extent on the rate of precipitation (e.g. Allen et al., 2008). Here, we show through geomorphic mapping and  $^{36}\text{Cl}$  exposure dating, that Mount Lebanon hosts glacial features and sediments that testify to the development of glaciers during the LGM in agreement with Messerli (1966), and we discuss how these results translate into the LGM climatic conditions of the Levant region.

## 2. Geomorphic and climatic setting of Mount Lebanon and the Cedars cirque

Mountain ranges in Lebanon (latitude  $\approx 34^{\circ}\text{N}$ ) formed as a result of compressive deformation across the Lebanese restraining bend of the Dead Sea Transform plate boundary (Elias et al., 2007) (Fig. 1b). Sharply bounded to the E by the Yammouneh fault, which is part of the Dead Sea plate boundary, Mount Lebanon is a 150-km-long NNE-SSW-trending mountain range. Both its width and elevation increase northeastward (Fig. 2a). The modern climate over Mount Lebanon results from the superimposition of the orographic effect (elevation up to 3000 m) on the Mediterranean influence (hot-dry summers and cool-wet winters). The monthly average temperature in Bcharre (the meteorological station closest to the studied sites; see Fig. 2a), 1430 m a.s.l., ranges from  $0^{\circ}\text{C}$  in January and February to  $17^{\circ}\text{C}$  in July and August. Annual precipitation is 924 mm, increasing up to 1400 mm in Mount Lebanon (Fig. 2a) (Cheddadi and Khater (2016) after Plassard (1981)), 85% of which occurs between November and March (Abi-Saleh and Safi, 1988). The impact of the orographic effect on the rates of precipitation is evidenced by the sharp decrease in precipitation between Mount Lebanon and the semi-arid to arid Bekaa Valley (Fig. 2a).

Our study area is located on Jabal El Makmal, the highest mountain of the Eastern Mediterranean – Levant coast culminating at around 3088 m a.s.l. in Qornet Es Sawda. The mountain top extends southwards as a  $\sim 70$  km plateau – Mnaitra Plateau (Fig. 2a). Structurally, this plateau corresponds to the flat limb of the west-dipping Mt-Lebanon monocline. The plateau bounds the Yammouneh fault and plate boundary along a 500-700-m-high escarpment separating Mt Lebanon from the Bekaa Valley (MLBV escarpment) (Daëron et al., 2007) (Fig. 2a–c). The surface of the plateau is carved into the 500-700-m-thick Sannine limestone formation of the early Upper Cretaceous (Walley, 1997), and is exposed to dominant winds blowing from the W (Maheras, 1988; Messerli, 1966). Its surface displays a poorly-channelized morphology marked by prominent evidence of karstic erosion

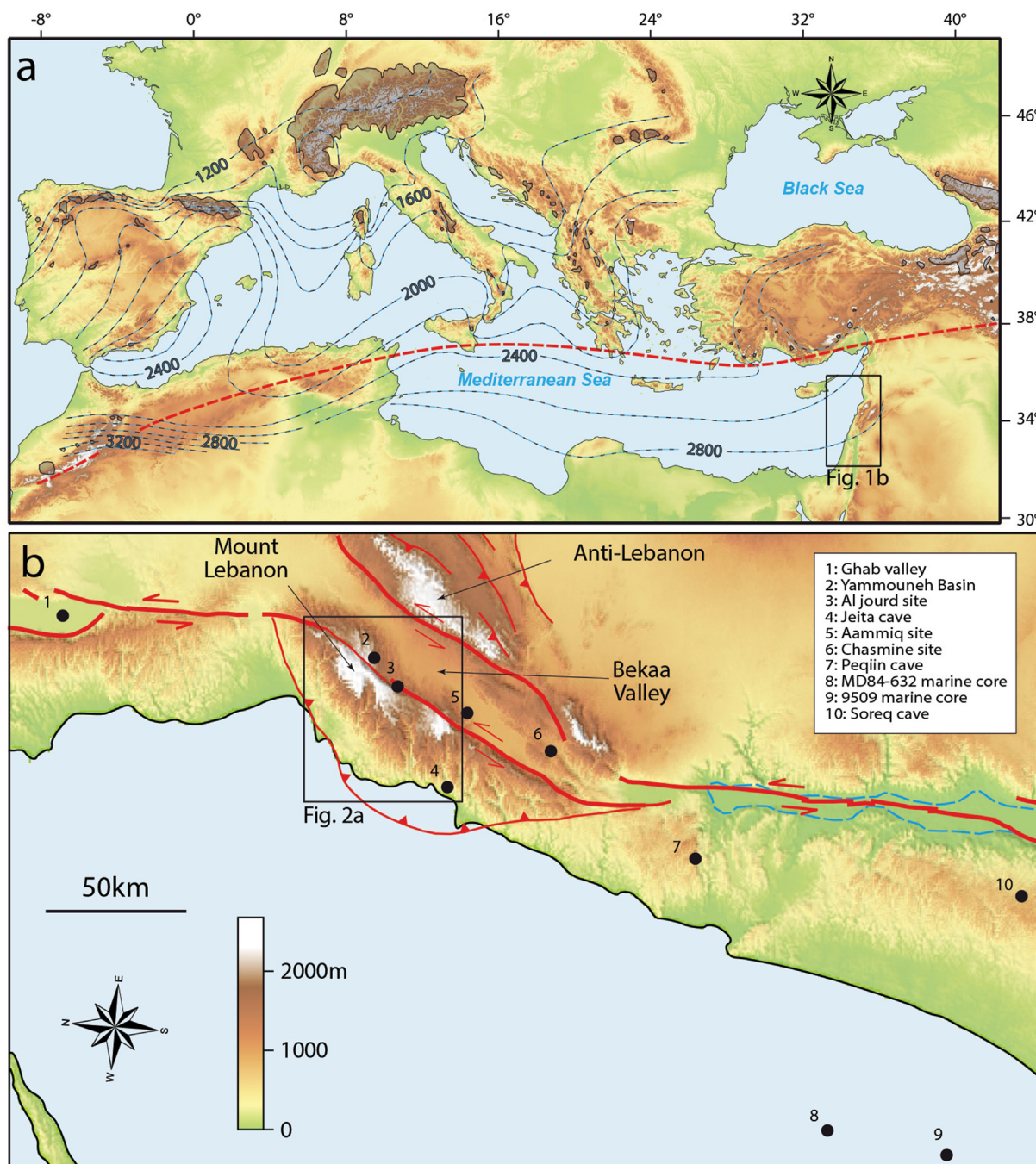


**Fig. 1.** Location of the study site in the context of previous paleo-climate records in the Mediterranean (a) Interpolated ELA (dashed black-blue lines) constructed based on local maximum advances of glaciers around the Mediterranean basin (Kuhlemann et al. (2008) completed by map of Messerli (1966) for the southeastern corner of the Mediterranean). Note that the highlighted ELA pattern is thus diachronic since some Mediterranean glaciers reached their maximum in the LGM (e.g. Turkey) while some other did in the Middle Pleistocene (Balkans, Greece). However, it still provides a broad view of the atmospheric structure during glacial conditions. The extent of LGM glaciers is shown in transparent black (after Allen et al., 2008; Ehlers and Gibbard, 2004; Kuhlemann et al., 2008). The dashed red line represents the southern limit of known LGM glaciers in the Mediterranean. (b) Shaded relief of the Levant region showing the location of the main paleo-climatic records discussed in the text. The main active faults are drawn in red after Daéron et al. (2007). The blue dashed line represents the extent of paleo-Lake Lisan. Topographic scale is the same in (a) and (b). (For interpretation of the references to color in this figure legend, the reader is referred to the Web version of this article.)

(numerous dolines in particular). When exposed at the western rim of the Mnaïtra plateau, the hard Sannine formation forms a prominent topographic step that follows a SSW-NNE trend parallel to both the Mediterranean shoreline and the axis of the monocline (Fig. 2a). This escarpment is locally dissected by the headward retreat of Mediterranean tributaries (Fig. 2a). Near the highest elevations of Mt Lebanon, the rim of the plateau deviates from its

SSW-NNE general trend, as it bends in the E-W direction along the upper course of the Qadisha River, to form the walls of the Cedars cirque (Fig. 2a–c).

The Cedars cirque is a major horseshoe-shaped incision (in map view), open to the west, extending for 10–12 km in E-W direction over the entire width of the Jabal el Makmal relief. It is 6–7 km wide with an area of about 28 km<sup>2</sup> (Fig. 2a–c). The floor of the

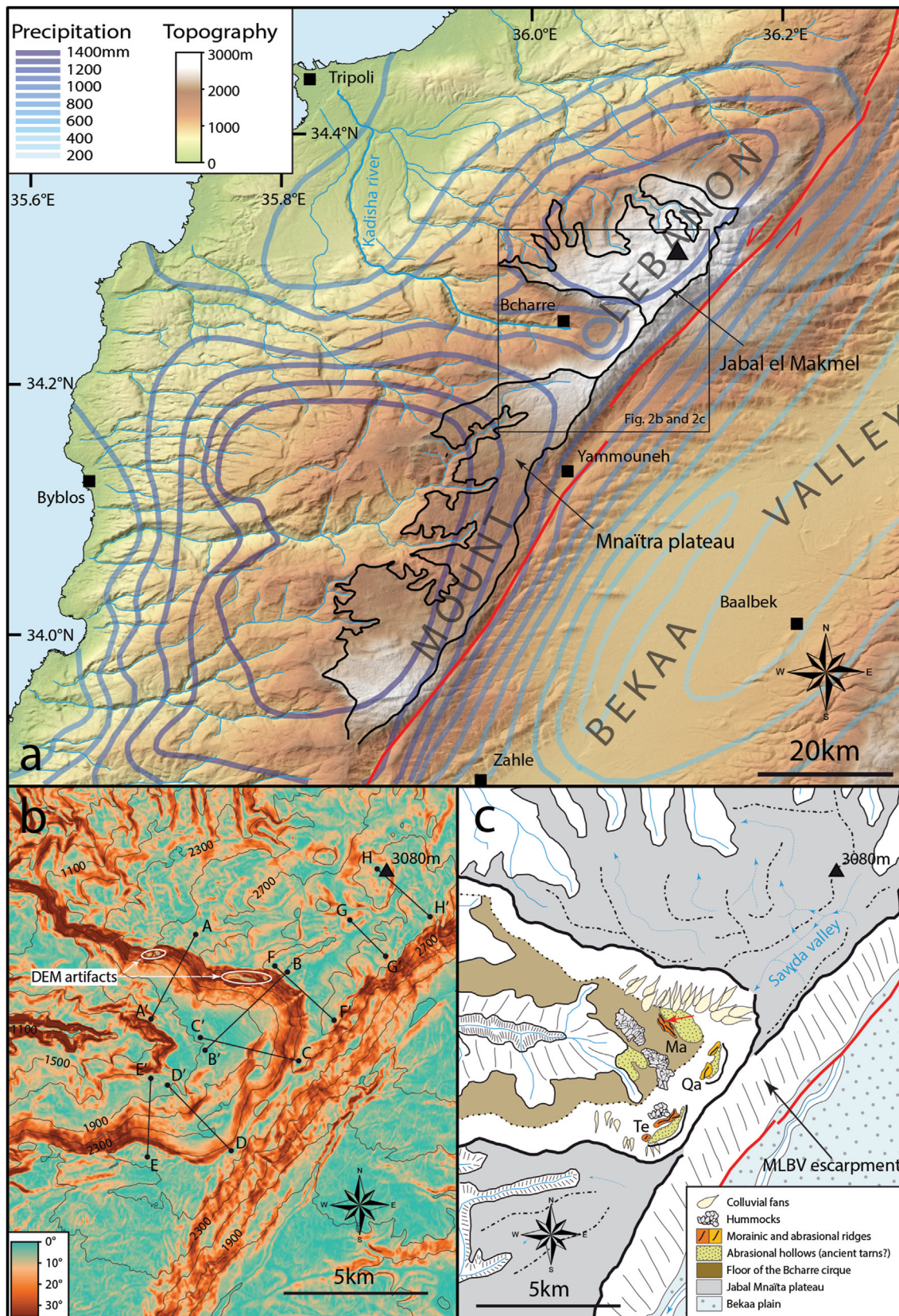


**Fig. 2.** Location of the study site in the context of local precipitation, topography and geomorphology. (a): Drainage network around Jabal el Makmel. Catchment limits are depicted with dashed black lines. The solid black line delineates Mt-Lebanon plateau. Precipitation contours are same as in Fig. 1b (Cheddadi and Khater (2016) after Plassard (1981)). Black triangles denotes the Qurnat as Sawda', the highest peak of Mount Lebanon (3088m). (b) Slope map of the Cedars cirque and surrounding areas, derived from a 20-m-DEM of Lebanon (i.e. SPOT DEM product extracted from SPOT 5 HRS stereoscopic data), 200-m interval elevation contours are superposed over the slope map. Black lines show location of transects of Fig. 4. (c) Geomorphic interpretation of the same area as in (b) based on field observations and the analysis of 2.5-m-SPOT imagery, 1:20,000 topographic maps, and the 20-m DEM of Lebanon.

cirque has an average elevation of 1900m, and is dissected by a 300–400-m-deep, E-W-trending canyon of the Qadisha river. It is separated from the plateau by a laterally continuous 600–900-m-high escarpment made of the resistant limestone of the Sannine formation (Figs. 2b, 3 b–d). The steepest topographic profile of this escarpment is generally concave upwards, with the slope increasing from 5° at the base to 30° at the top (Figs. 2b and 4a). The sloping surface of the escarpment is relatively smooth and fairly continuous, covered by numerous colluvial fans (Figs. 2c, 3c–d). According to the present topography, there is only one point of hydrological connection between the plateau and the cirque. It corresponds to the outlet of a 4–5-km-long, flat bottom U-shaped valley (hereafter referred to as the Sawda valley; Fig. 3a and e) floored by sorted clasts typical of periglacial conditions (i.e. upfreezing, Anderson (1988)). The Sawda valley occupies a special position within the Mnaitra plateau since it is the only thalweg which is not oriented along the NNW-SSE regional steepest gradient. Its upper reach is located on the SE side of the Qornet Es Sawda (Fig. 2c), making the Sawda valley the only leeward portion of the plateau and hence favoring accumulation of ice there (Messerli, 1966). The valley is oriented parallel to the MLBV escarpment (Fig. 2c) and is characterized by a very gentle topographic gradient (less than 1°) at elevation between about 2950 and 2800 m a.s.l. It terminates at the NE edge of the Cedars cirque in the form of a 100–150-m-deep U-shaped notch suspended above the cirque floor (Fig. 2c, and blue arrow in Fig. 3b)

Field observations and the analysis of 1:20,000 topographical maps and 2.5-m-resolution SPOT images allowed a distinctive top-down series of landforms, characteristic of glacier formations, to be mapped at three distinct locations within the Cedars cirque (Manhale, Qandil, and Terkmen sites in Fig. 2). Each series hosts one, or a group of few, 10-m-high 100-m-wide curvilinear morainic ridges (Fig. 3b, d, 3e, and 3f) that separates a depressed clay-rich level terrain uphill (Fig. 3b, d, and 3f) from a field of hummocks downhill (Fig. 3c). However, despite these similarities, there is a fundamental difference between Manhale and the two other sites. At Terkmen and Qandil, the typical landform succession rests on the steep cirque wall (Fig. 2b and c), such that the topographic cross-section features a prominent abrasional hollow isolated by a downstream ridge (Fig. 4b). This clay-rich depression is almost topographically closed, and possibly reveals an ancient pro-glacial lake (Figs. 2c and 3b). At Manhale, however, the landform succession covers the gently sloping floor of the Cedars cirque, such that the topographic signature is more subdued and the clay-rich level terrain has a broader extension in the upstream direction (Figs. 2c, 3d and 3f, and 4b). In addition, the Manhale succession lays immediately below the U-shaped notch outlet of the Sawda valley (Fig. 2c), which suggests that the Manhale moraine might have been emplaced by a former glacier originating from the Sawda valley and cascading on the northeastern wall of the Cedars cirque.

At Manhale and Terkmen (but not at Qandil), large pieces of limestone conglomerates, composed of moderately to well-rounded 1–50-cm pebbles and cemented by secondary calcite, are exposed at the surface of the ridges (Fig. 3h). These characteristics are commonly observed at the surface of limestone moraines (Hughes et al., 2010). The core of the westernmost Manhale ridge, exposed in a large man-made excavation, is a matrix-supported, unsorted, and unstratified diamicton, composed of rounded to sub-rounded cobbles and pebbles of limestones floating within a white silty matrix (Fig. 5). Boulders are only occasionally found and

never exceed 1 m. The upper cemented horizon is thin, and does not propagate deeper than a few tens of centimeters below the surface (Fig. 5). Although the core of the Terkmen ridges is not excavated, we assume, based on the similar surface morphology and composition, that it is composed of the same diamicton as that in Manhale. On the other hand, the absence of the cemented conglomerate at the surface of the Qandil ridge (see different color code in Fig. 2c) suggests the latter might represent a bedrock abrasional ridge without deposition.

The clear evidence of abrasional landforms (U-shaped Sawda valley, and small cirques at Terkmen and Qandil) at an elevation compatible with known LGM glaciers in climatically similar regions nearby (e.g. Sarikaya et al., 2009) (Fig. 1a), and their association with diamicton sediments typical of glacial tills, strongly suggest that the landform successions observed within and above the Cedars cirque are of glacial origin. Several possible glacial origins have been proposed for hummocks, such as the melting of detached patches of ice during glacier retreat (e.g. Bennett and Boulton, 1993; Bennett, 1994), or the subglacial deformation of older till deposits under the overburden pressure of stagnant ice (Boone and Eyes, 2001; Hodgson, 1982). However, in the present case, where karst is likely to play a major role, it is also possible that the hummocky topography formed as a result of suffusion processes, during which till sediments are evacuated through underlying karstic pipes (Çiner et al., 2019; Ford and Williams, 2013).

That the Mount Lebanon hosts evidence of past glaciation is consistent with earlier work of Messerli (1966) in this area. Given their orientation relative to the surrounding topography (Fig. 2c), the Manhale, Terkmen, and Qandil ridges most likely represent frontal moraines, which thus record a maximum extent of the former glaciers (Refsnider et al., 2007). In the next section, we focus on the Manhale morainic ridges, for which we attempt to derive an age of emplacement through  $^{36}\text{Cl}$  Cosmic Ray Exposure dating.

### 3. $^{36}\text{Cl}$ Cosmic Ray Exposure dating of the Manhale ridge

The chronology of emplacement of the Manhale ridge was established through  $^{36}\text{Cl}$  Cosmic Ray Exposure (CRE) dating of the diamicton deposit.  $^{36}\text{Cl}$  is a cosmogenic nuclide produced by the interactions between cosmic ray particles and specific target elements, the most abundant ones in limestone being Ca and Cl. Like any other cosmogenic nuclide, the variability of the rate of  $^{36}\text{Cl}$  production at the Earth's surface essentially depends on the latitude, altitude, and topographic shielding of the sampled site, and can be determined from scaling schemes (e.g. Stone, 2000).  $^{36}\text{Cl}$  is also a radioactive nuclide, with a decay constant of  $2.30 \times 10^{-6} \text{ yr}^{-1}$ .

For a given site, the concentration of  $^{36}\text{Cl}$  in a surface sample is a function of the local production rate ( $P$ ), the age of surface exposure ( $t$ ), the rate of denudation ( $\epsilon$ ), and the  $^{36}\text{Cl}$  inheritance ( $C_0$ ) (i.e. the  $^{36}\text{Cl}$  inventory contained in the sample at the time of emplacement of the sampled landform). Deriving robust constraints on the age of exposure therefore requires to simultaneously solve for the three latter unknowns. The best way to achieve this is to collect several samples along a depth profile (Braucher et al., 2009; Hidy et al., 2010). This is because secondary neutrons and muons, which are the cosmic ray particles responsible for the cosmogenic production, are attenuated with depth following a specific pattern as a function of denudation and inheritance (Schimmelpfennig, 2009). Any collection of (concentration, depth) data thus has the potential of constraining the most likely ( $t$ ,  $\epsilon$ ,  $C_0$ ) triplet associated with the

Ma = Manhale, Qa = Qandil, Te = Terkmen. MLBV escarpment = MountLebanon-BekaaValley escarpment. Yellow versus orange ridges refer to the abrasional versus depositional nature of the mapped ridges. Red arrow locates the  $^{36}\text{Cl}$  depth-profile. The internal topography of the plateau is represented by the watershed ridges (thick black dashed lines) and thalwegs (dashed blue arrows). (For interpretation of the references to color in this figure legend, the reader is referred to the Web version of this article.)

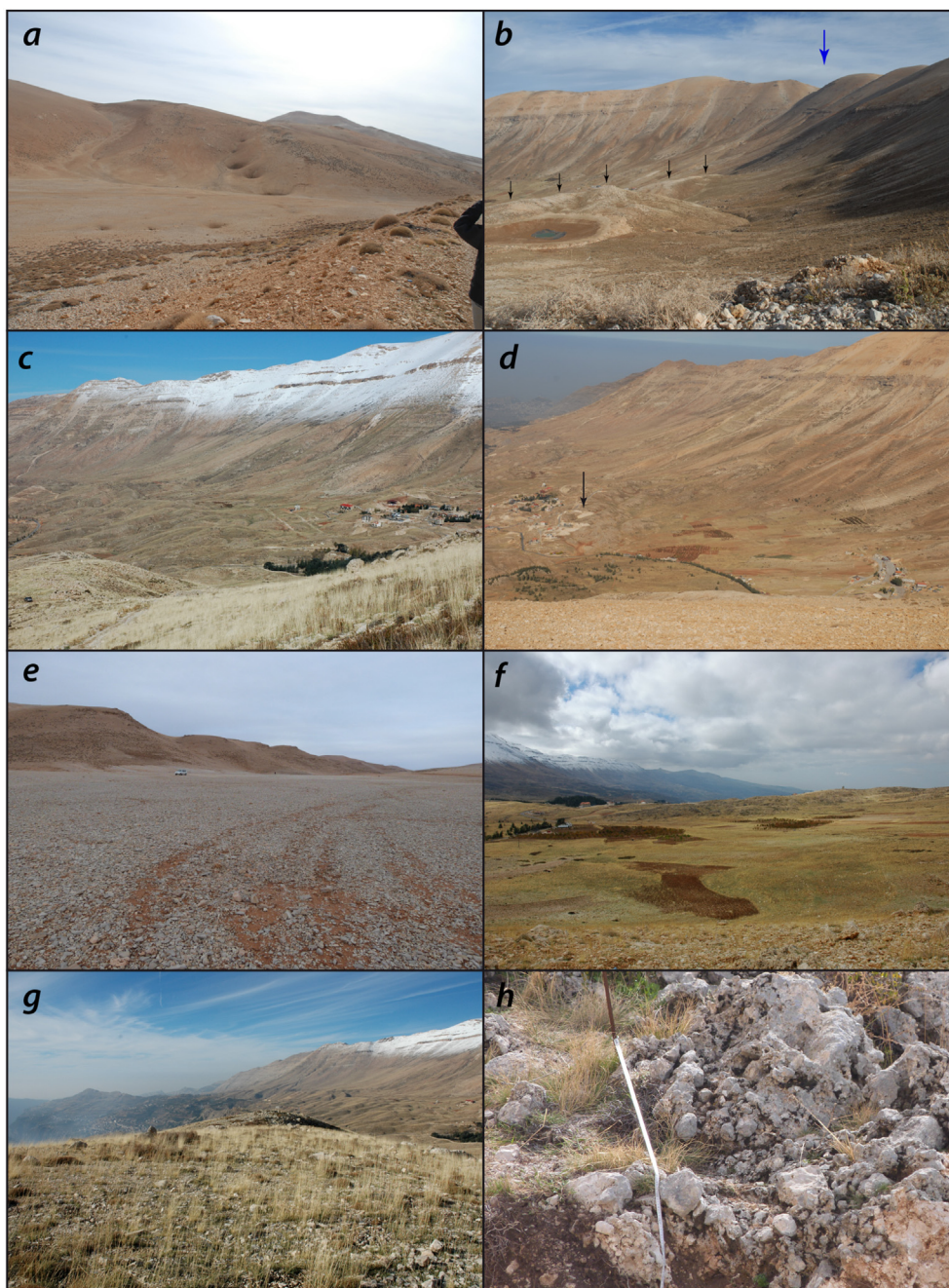


**Fig. 3.** Field pictures: (a) SE view of the Sawda valley (note the presence of sinkholes at the base of the slopes), (b) the Qandil ridge (black arrows) and the northern and eastern walls of the Cedars cirque in the background (looking N). The blue arrow shows the outlet of the Sawda valley, (c) view looking NNW showing the fields of hummocks in Manhale and the northern wall of the Cedars cirque in the background, (d) the Manhale ridges (black arrow shows the location of the excavation where the  $^{36}\text{Cl}$  depth profile was sampled) looking WNW, and the cultivated clay-rich depression on the back, (e) the flat bottom of the Sawda valley floored by sorted (non-patterned) clasts, (f) WSW view with the Manhale ridges (in the middle-background) and its associated clay-rich depression (in the foreground), (g) the Terkmen morainic ridge looking NW, (h) the morainic deposit cemented by secondary calcite on top of the  $^{36}\text{Cl}$  depth-profile of Fig. 5. (For interpretation of the references to color in this figure legend, the reader is referred to the Web version of this article.)

sampled landform (Braucher et al., 2009; Hidy et al., 2010).

For this purpose, a depth profile was sampled along the vertical subsurface wall of a newly excavated construction site in the Manhale ridge (Fig. 5). Eighteen samples, each made of 10–20-cm-large individual pebble, were collected at depths between 0 and 975 cm beneath the ridge axis in order to minimize surface denudation. The major source of uncertainty in modeling cosmogenic depth profiles resides in the estimation of the density of the material, across which the cosmic ray particles are attenuated (Braucher et al., 2009). For this, we first measured the density of the

clay matrix by weighing a 1-dm<sup>3</sup>-volume of matrix in the field. The measured matrix density is 1.2 g cm<sup>-3</sup>, approximately half the 2.7 g cm<sup>-3</sup> density of the pebbles. We have then estimated the proportion of pebbles within the diamicton to about 30% according to field photographs of the outcrop, yielding a bulk density of approximately 1.65 g cm<sup>-3</sup>.

Pebble samples were crushed, and the 250–500- $\mu\text{m}$  fraction was leached, then dissolved following the procedure of Stone et al. (1996), modified by Schlagenhauf et al. (2011). After complete dissolution, the samples were spiked with a known amount of

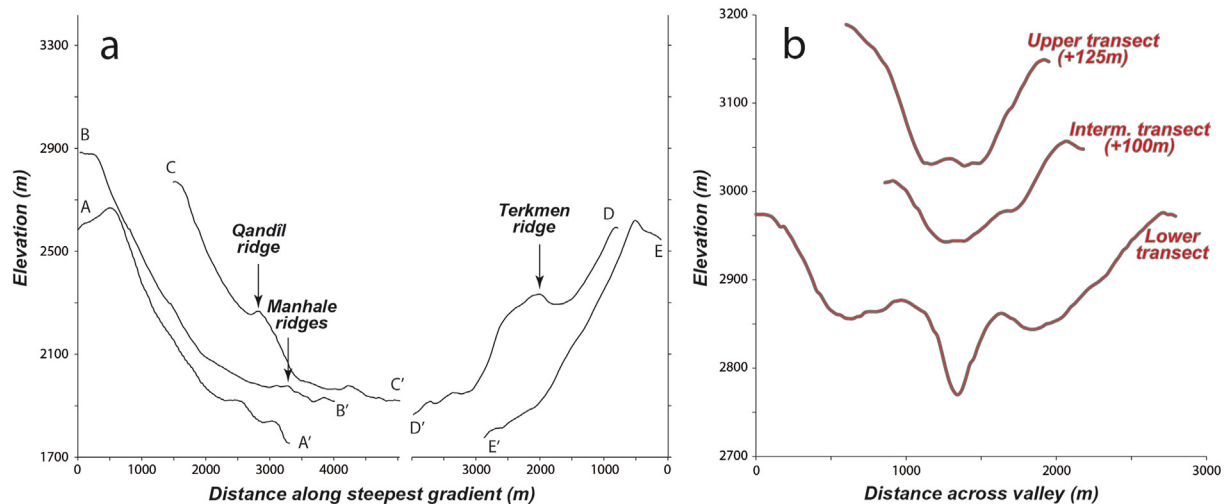


**Fig. 4.** Topographic profiles (extracted from the 20-m-DEM of Lebanon; see Fig. 3a for location) across the walls of the Cedars cirque (a) and across the Sawda valley (b). Note the abrasional hollows behind the Qandil and Terkmen ridges (profiles DD' and CC' in (a)), and the U shape of the Sawda valley (b). Values in brackets in (b) indicate the magnitude of upward shift which has been applied to the intermediate and upper profiles for the sake of clarity.

isotopically enriched stable chloride carrier to allow for simultaneous Cl and  $^{36}\text{Cl}$  determination by isotope dilution (Schlagenhauf et al. (2011) and references therein). Cl was then precipitated as AgCl. Both the  $^{36}\text{Cl}$  and Cl concentrations were measured at the national French AMS facility ASTER (CEREGE, Aix-en-Provence), and normalized to a  $^{36}\text{Cl}$  standard prepared by K. Nishiizumi (KNSTD1600, with a given  $^{36}\text{Cl}/^{35}\text{Cl}$  value of  $(2.11 \pm 0.06) \times 10^{-12}$ ; Sharma et al., 1990; Fifield et al., 1990). The analytical uncertainties included counting statistics, machine stability and blank correction. Calcium concentration was measured in aliquots by ICP-AES analyses.

The obtained  $^{36}\text{Cl}$  concentrations vary from  $6.267 \times 10^4$  to  $1.548 \times 10^6$  atoms per gram of rock (Fig. 5 and Table 1) with a clear exponential decrease of  $^{36}\text{Cl}$  concentrations with depth (Fig. 5), suggesting that deposition occurred over a time interval that is short relative to the time of exposure, and also that there has been insignificant vertical mixing of pebbles within the diamicton. In other words, the deposit was built over a discrete time, and it has remained relatively stable since then. The depth profile is modeled using a recently developed  $^{36}\text{Cl}$ -exposure-calculator (Schimmelpfennig et al., 2019), which makes use of Markov chain Monte Carlo sampler of Goodman and Weare (2010) to construct posterior distributions of the model parameters ( $t$ ,  $\epsilon$ ,  $C_0$ ). A value of  $48.8 \pm 4.8$  atoms  $\text{g}^{-1} \text{a}^{-1}$  (Stone et al., 1996) was used as the spallation production rate at sea level and high latitude, which was scaled to the sampled site using the Lal (1991), modified by Stone (2000), scaling scheme. Muonic production calculations are performed using the equations of Heisinger et al. (2002a, 2002b) adopting the approach of Balco (2017) to calculate muon production at a particular altitude and subsurface depth. The calculation includes a mean chemical composition for all the samples (Supplementary Table 1) derived from the analysis of 5 samples over the whole profile. The production rate along this profile is reasonably well constrained owing to the low Cl content of the sampled pebbles (Table 1). For the field-estimated density of  $1.65 \text{ g cm}^{-3}$ , the depth-profile modeling yields an exposure age of  $25.4 \pm 3.1 \text{ ka}$ , compatible with the Last Glacial Maximum, and requires relatively low rates of denudation (about  $20.9 \pm 11.2 \text{ mm/ka}$ ), (Table 2). These outputs include the uncertainties associated to the production rate, as they were propagated through the Bayesian inversion. Uncertainties resulting from

the estimated density have been addressed by modeling the profile using different proportions of pebble/matrix (Table 2).

#### 4. Glacier reconstruction, ELA, and paleo-climatic constraints

The geomorphological evidence presented in section 2, as well as the LGM age control on the emplacement of the diamicton at Manhale (section 3), collectively support the hypothesis that the landform successions observed at the three sites are largely derived from the action of former glaciers through abrasional, depositional, and melting processes. At Terkmen and Qandil, these glaciers could not have been much larger than  $1.0\text{--}1.5 \text{ km}^2$ , as testified by the limited upstream glacial cirques catchments (Figs. 2c and 3b). It thus requires the vertical extension of the glaciers to be small, picturing them as small ice caps developed from areas of snow accumulation on-the-spot. Therefore, the 2300–2400-m-elevation of these two small cirques (Figs. 2b and 3a) should provide a reasonable estimate of the former local ELA and hence strongly suggests that these two glaciers were active broadly at the same time.

On the other hand, the Manhale morainic ridges clearly lay at lower elevation than those at Terkmen and Qandil (about 300–350-m below), but must have had a much larger upstream catchment (about  $9.15 \text{ km}^2$ ). This is because it had to include the U-shape Sawda valley, suspended on top of the Cedars cirque and stretching up to about 3000 m (Fig. 2b and c). Therefore, the 2000-m-elevation of the Manhale moraines yields only a minimum estimate of the LGM ELA, since the downward extent of a glacier below the ELA is likely to scale with the accumulation area (i.e. the glacier area above the ELA) (Pellitero et al., 2015).

We have quantitatively tested these first-order ELA estimates for the three glaciers by combining the *GlaRe* (Pellitero et al., 2016) and *ELA calculation* (Pellitero et al., 2015) toolboxes (both of them running in ArcGIS software). The equilibrium profile of each paleo-glacier was first reconstructed based on their inferred geometries (shown in Fig. 6a) using *GlaRe*. The geometry of the Manhale glacier was inferred from both the trimlines of the Sawda valley and the position and extent of the frontal moraines. The main uncertainty associated with this reconstruction is on the left bank of the Sawda valley, where the trimline is not continuous, and sometimes divides

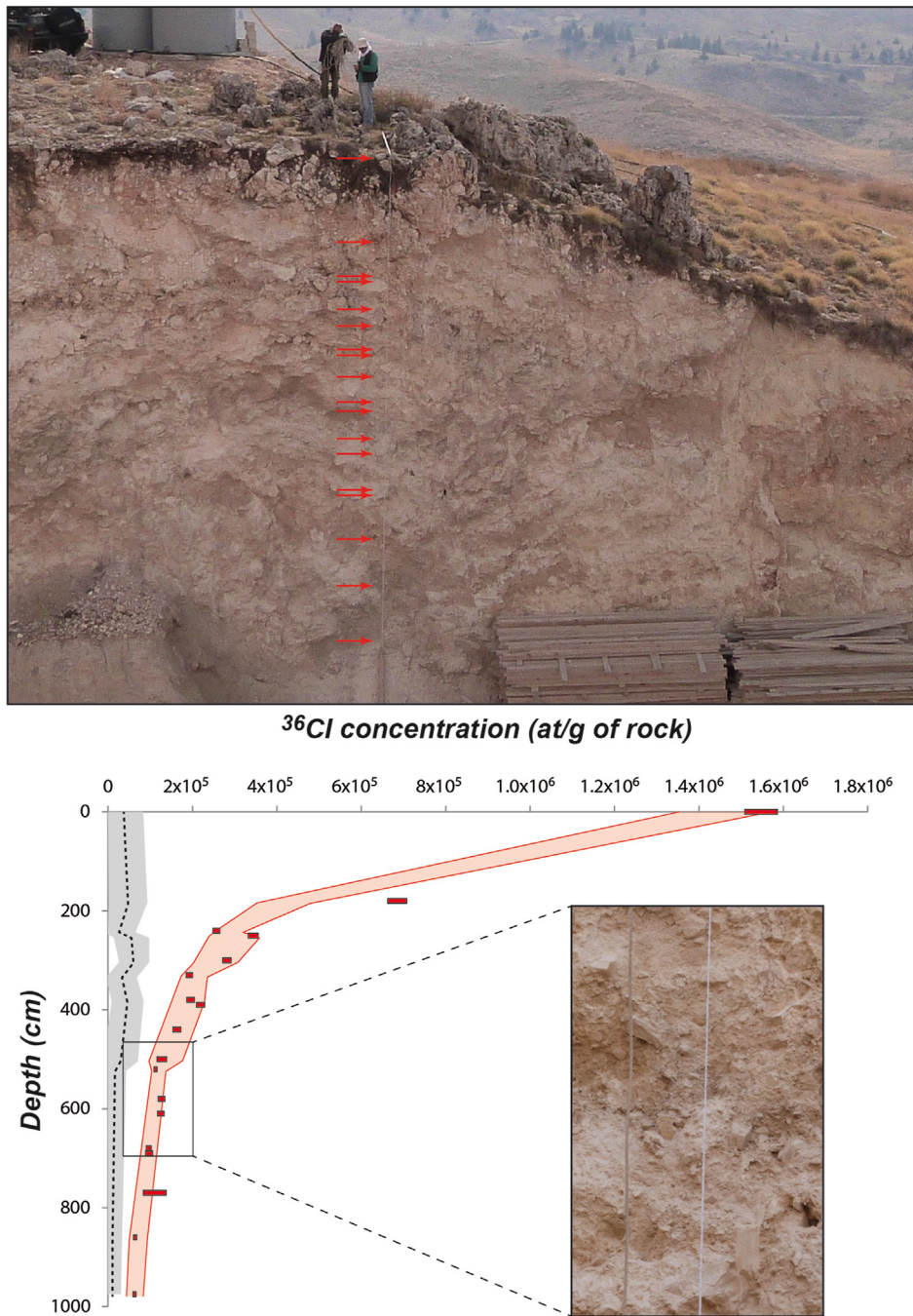


**Fig. 5.** (Above) SE view of the Manhale moraine excavation site wall, with position of collected samples indicated by red arrows. (Below) The graph of measured <sup>36</sup>Cl concentrations plotted against depth of the corresponding sample using same vertical scale as the field picture. Red boxes are for sample's concentration where box width relates to the 1σ uncertainty. Red envelope represents the 1.6-density model output including 2σ uncertainties. The breaks in the exponential trend reflect the effect of sample-specific concentrations of target elements. Black dashed curve and gray envelope represent the sample-specific inheritance and associated 2σ uncertainties yielded by the Monte Carlo inversion. The inset picture is a close-up of the diamicton deposit between 5 m and 7 m depth. (For interpretation of the references to color in this figure legend, the reader is referred to the Web version of this article.)

into two sub-parallel branches separated from each other by up to 300 m. In the *GlaRe* simulations, two distinct geometries of the paleo-glacier were thus used to reconstruct the equilibrium profile (*smaller* and *larger* glacier; see solid and dashed lines in Fig. 6a). Similarly, two extreme geometries were used for the Terkmen and Qandil paleo-glaciers, one restricted to the inferred pro-glacial lake, and the other extending up to the southeastern limit of the Cedars cirque (Fig. 6a).

The glacier surface outputs yielded by the *GlaRe* simulations were then used to calculate the corresponding ELA in the *ELA calculation* toolbox using the widely used Accumulation Area Ratio (AAR) method (Pellitero et al., 2015). We considered AAR ratios ranging between 0.65 and 0.7, thereby bracketing the widely accepted value of 0.67 (Pellitero et al., 2015; see also Kern and László, 2010). The obtained ELAs range between 2410 and 2430 m when considering the Qandil ridge, 2395 and 2425 m when

**Table 1**

Site description, general sample information, measurements ( $^{36}\text{Cl}/^{35}\text{Cl}$  and  $^{35}\text{Cl}/^{37}\text{Cl}$  ratios and chlorine and CaO concentrations) and calculated  $^{36}\text{Cl}$  and chlorine concentrations. Whole-rock composition can be accessed through online Supplementary Table.

Elevation	Latitude	Longitude	Shielding	$^{36}\text{Cl}$ blank corr.				
2006 m	34.24969	36.0517	0.986	5.8 $10^4$ atoms				
Samples	Depth (cm)	Dissolved weight (g)	Mass of Cl in spike (mg)	$^{36}\text{Cl}/^{35}\text{Cl}$ ( $\times 10^{-14}$ )	$^{35}\text{Cl}/^{37}\text{Cl}$	$^{36}\text{Cl}$ ( $\times 10^4$ at/g)	Cl (ppm)	CaO (%)
MAP11-1	0	82.63	2.37	354.31 $\pm$ 7.63	9.74 $\pm$ 0.02	154.7 $\pm$ 3.9	11	55.9
MAP11-20	180	83.86	2.39	132.77 $\pm$ 3.83	7.29 $\pm$ 0.02	68.5 $\pm$ 2.3	17	55.7
MAP11-3	240	83.92	2.36	71.42 $\pm$ 2.27	16.28 $\pm$ 0.04	25.7 $\pm$ 0.9	5	55.0
MAP11-4	250	96.68	2.36	84.02 $\pm$ 2.63	8.15 $\pm$ 0.02	34.4 $\pm$ 1.2	12	55.9
MAP11-21	300	81.55	2.38	64.49 $\pm$ 2.08	10.10 $\pm$ 0.03	28.1 $\pm$ 1.0	10	56.6
MAP11-5	330	76.5	2.36	32.55 $\pm$ 1.09	6.76 $\pm$ 0.09	19.3 $\pm$ 0.8	21	44.2
MAP11-6	380	70.05	2.35	28.74 $\pm$ 1.19	6.36 $\pm$ 0.08	19.5 $\pm$ 0.9	26	46.7
MAP11-7	390	76.66	2.37	21.32 $\pm$ 0.77	4.53 $\pm$ 0.02	21.9 $\pm$ 1.0	55	44.0
MAP11-8	440	51.23	2.37	15.41 $\pm$ 0.83	5.67 $\pm$ 0.04	16.3 $\pm$ 1.0	46	44.5
MAP11-9	500	74.5	2.38	16.36 $\pm$ 1.41	5.42 $\pm$ 0.05	12.7 $\pm$ 1.1	35	45.7
MAP11-10	520	77.07	2.38	23.17 $\pm$ 0.70	9.03 $\pm$ 0.08	11.2 $\pm$ 0.4	13	47.0
MAP11-11	580	65.87	2.38	9.40 $\pm$ 0.52	4.31 $\pm$ 0.03	12.7 $\pm$ 0.8	76	34.8
MAP11-12	610	51.37	2.38	9.81 $\pm$ 0.58	4.99 $\pm$ 0.01	12.5 $\pm$ 0.8	62	39.5
MAP11-14	680	53.02	2.37	7.34 $\pm$ 0.40	4.80 $\pm$ 0.02	9.6 $\pm$ 0.6	67	32.9
MAP11-13	690	51.33	2.38	6.29 $\pm$ 0.50	4.51 $\pm$ 0.01	9.7 $\pm$ 0.8	84	32.3
MAP11-15	770	4.76	2.9	2.02 $\pm$ 0.44	20.82 $\pm$ 0.06	11.1 $\pm$ 2.7	69	33.0
MAP11-16	860	69.24	2.39	7.77 $\pm$ 0.44	5.48 $\pm$ 0.01	6.4 $\pm$ 0.4	37	38.2
MAP11-17	975	77.6	2.4	6.73 $\pm$ 0.34	4.73 $\pm$ 0.01	6.3 $\pm$ 0.4	48	42.2

**Table 2**

Results of profile modeling using Bayesian inversion (3,000,000 iterations). RMS (Residual Mean Square) shows no convergence towards reasonable density values, implying that model outputs cannot be used to constrain the density.

Density ( $\text{g}/\text{cm}^{-3}$ )	Exposure-age (ka)	Erosion-rate (mm/ka)	RMS
1.2	20.1 $\pm$ 0.9	6.3 $\pm$ 6.3	28
1.4	21.7 $\pm$ 1.4	10.4 $\pm$ 8.1	37
1.6	25.4 $\pm$ 3.1	20.9 $\pm$ 11.2	62
1.8	31.2 $\pm$ 4.5	29.9 $\pm$ 10.4	85
2.0	37.9 $\pm$ 6.3	33.9 $\pm$ 9.2	103

considering the Turkmen morainic ridge, and 2310 and 2650 m when considering the Manhale morainic ridges. As expected, the ELA of the Turkmen and Qandil paleo-glaciers is close to the elevation of the cirques, and this is irrespective of the chosen glacier geometries, as the *smaller glacier* and *larger glacier* end-members yield ELAs that differ by only 20–30 m. In addition, the ELAs of the Turkmen and Qandil paleo-glaciers are undistinguishable from each other within uncertainties (about 2400 m), which strongly supports the view that the two groups of landforms record a single glacial event. The ELA obtained for the *smaller* Manhale paleo-glacier (2310–2430 m) is also compatible with the 2400 m ELA estimated for the other two. Even the *larger glacier* end-member with slightly higher values (2390–2650 m) is consistent within uncertainties. The internal consistency between the ELAs obtained from the three paleo-glaciers within a small geographic area strongly suggests that they all record a single glacial event, associated with an ELA at about 2400 m (i.e. the *smaller glacier* end-member is preferred over the *larger glacier* end-member for the Manhale paleo-glacier).

The obtained ELA interval was further used to constrain paleoclimatic parameters. Specifically, the glacier mass balance at the reconstructed ELA (2310–2650 m) was computed for various changes in precipitation and temperature relative to modern conditions, and using a degree-day model. Degree-day models are based on the assumption that when the air temperature is above the melting point, the ablation rate of a glacier is proportional to the temperature (Braithwaite and Olesen, 1989). Accumulation is obtained as the product of monthly precipitation and monthly probability of freezing, with the latter estimated from the

assumption that temperatures within a month are normally distributed with a standard deviation of 4 °C (Braithwaite, 1984). Yearly ablation is obtained as the product of the positive degree-day sum and the degree-day factor, where the positive degree-day sum is the sum of positive air temperatures (Braithwaite and Zhang, 2000) calculated assuming a sinusoidal temperature variation throughout the year (Braithwaite et al., 2006; Brugger, 2006; Hughes and Braithwaite, 2008). The degree-day factor is a quantity that describes how fast the melting of snow (or ice) occurs along with increasing temperature above the melting point (Braithwaite and Olesen, 1989).

Our model used modern climate conditions (monthly temperature and precipitation) taken from an observation time range of 21 years between 1949 and 1970 (Plassard, 1981) at Bcharre (1430 m a.s.l.) located 5–6 km away from the paleo-glaciers ELA. Temperatures were scaled to the altitude of the glaciers using the standard atmospheric lapse-rate (6.5 °C km<sup>-1</sup>) (Barry and Chorley, 2009). Monthly precipitation was increased by a factor of 1.10–1.15 relative to the Bcharre data, in order to account for the 100–150 mm difference in the annual precipitation observed between Bcharre and the area of the reconstructed paleo-glaciers (Fig. 2a). The explored space of paleoclimatic conditions includes a range of temperature cooling (T) between 1 and 14 °C, and a factor of precipitation change relative to present (FP) varying from x0.1 to x3.0. We applied a degree-day model for snow (most appropriate for exploring conditions at the ELA; Hughes and Braithwaite, 2008; Braithwaite and Raper, 2007) to these paleoclimatic conditions using an empirically constrained conservative interval of 4.1  $\pm$  1.5 mm/day/°C for the degree-day factor (Braithwaite, 2008). We have neglected accumulation through refreezing of melt water, which is justified by the fact that the annual temperature at the reconstructed ELA is rather high (Braithwaite et al., 2006): +2.5 °C today (and about -8 °C at the time of moraine emplacement, see section 5.2). The zero-mass-balance contours derived from both the preferred (2400 m) (thick black curve) and extreme bounds (2310 and 2650 m) (curves bounding dark gray envelope) of the ELA, and for the preferred degree-day factor of 4.1 mm/day/°C, are provided in the (T; FP) plot of Fig. 6b. The curves bounding the light gray envelope consider the extreme bounds of the degree-day factor. For each tested reconstruction (i.e. a given ELA associated to a given value of the degree-day factor), the corresponding curve captures

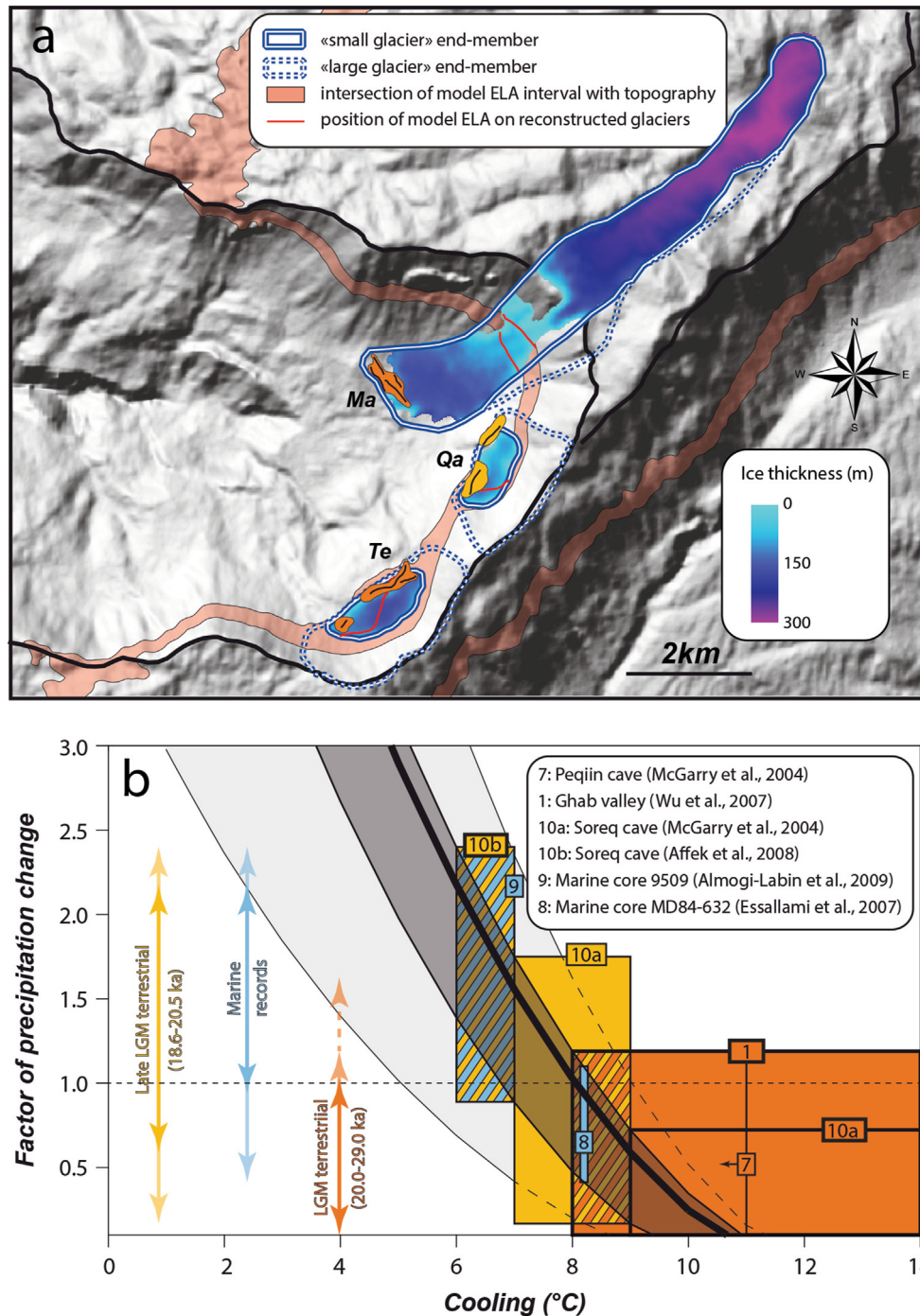


**Fig. 6.** ELA reconstructions and paleoclimatic implications. (a) The results of glacier and ELA reconstructions are summarized onto the shaded relief of the Cedars cirque. The ice thickness of the three glaciers comes from the simulations performed by the GlaRe toolbox of Pellitero et al. (2016). Ma = Manhale, Qa = Qandil, Te=Terkmen. (b) ( $\Delta T$ ; FP) plot. The transparent black envelope represents the changes in precipitation and temperature relative to modern conditions required to depress the LGM ELA into the conservative interval constrained from our simulations (as obtained from a degree-day model). Gray envelope is the same but also includes sensitivity to variations in degree-day factor of snow (from 2.6 to 5.6 mm/d/K). The thick black line depicts the preferred ELA (see text for more informations). The rectangular boxes have been constructed based on paleo-temperature estimates of the Levant region (see inset for references) and their compatibility with the ( $\Delta T$ ; FP) plot, and are color-coded according to the type of records (orange: Early LGM terrestrial record; yellow: Late LGM terrestrial record; blue: marine records). The double arrows denote the range of FP constrained by these boxes using either the gray envelope (dashed transparent arrow, only shown for orange color code), or the black envelope (transparent arrows), or the thick curve (non-transparent arrows). Hatched areas correspond to overlapping of two types of records. (For interpretation of the references to color in this figure legend, the reader is referred to the Web version of this article.)

the space of (T; FP) solution needed to sustain the reconstructed glacier. Paleo-climatic implications will be discussed in the next section.

## 5. Discussion

### 5.1. Presence of LGM glaciers on Mount Lebanon

The presence of LGM glaciers on Mount Lebanon is demonstrated by several lines of arguments. First, prominent abrasional landforms are observed, such as the U-shape Sawda valley and the over-deepening associated with former pro-glacial lakes at Terkmen and Qandil. Second, typical landform successions suggestive of melting/depositional processes are observed at the three studied localities (abrasional hollows, depositional or abrasional slope-orthogonal ridges, and fields of hummocks), and culminate with more than 10-m-thick diamicton deposit that forms the Manhale morainic ridges. Third,  $^{36}\text{Cl}$  dating of the Manhale diamicton demonstrates that these ridges were emplaced in a time interval consistent with the Last Glacial Maximum. Fourth, the Equilibrium Line Altitude required to sustain these paleo-glaciers (about 2400 m) matches with the LGM ELA reconstructions at similar latitudes in the Mediterranean (Fig. 1a).

Even if diamicton could also be associated to landslide sediments, the age of the deposit (LGM), and its spatial restriction to specific sites in the absence of fresh scars on the walls of the Cedars cirque rule out a non-glacial origin for the ridge deposits observed at Manhale. In addition, the Manhale group of ridges has an oblique linear trend relative to the local orientation of the cirque wall (Fig. 2c), which would not be expected if they had resulted from landsliding. In addition, it is worth noting that the glacial landforms are restricted to the W-facing wall of the Cedars cirque (Fig. 2c), suggesting that the causative agent of erosion and sedimentation did not affect the rest of the cirque, which has yet a similar geology and morphology. As depicted in Fig. 6a, this observation is strongly consistent with the reconstructed ELA, since only the eastern part of the Cedars cirque reaches elevations that are significantly above the 2400-m-contour, a condition necessary for snow accumulation from year to year, and glacier formation. Another possible explanation might be that the ELA was locally reduced on the W-facing side of the cirque because of higher rates of snow accumulation, resulting from the effects of the dominant winds blowing eastward from the Mediterranean (Maheras, 1988). In the latter case, the inferred 2400-m-ELA should be only used with caution when deriving paleo-temperature and paleo-precipitation. Specifically, for a given glacier extension and for a fixed temperature, the equilibrium precipitation should be reduced relative to the estimates derived in section 4, to an extent that would depend on the fraction of excess snow brought by wind transport from external sources (Hughes et al., 2006; Styllas et al., 2018).

The relatively smooth landscape of the Mnaitra plateau and Sawda valley at elevations well above the reconstructed ELA might seem surprising. We think that this particular morphology has resulted from the combined effect of wind and karst. The exposition of the plateau to dominant winds might indeed have hampered the accumulation of ice as already proposed by Messerli (1966). Accordingly, the leeward Sawda valley would have been the only portion of the plateau that allowed the development of a small glacier. Although the smooth morphology of the Sawda valley is somewhat atypical (subdued trimlines in particular), it is consistent with the landscapes observed in areas that underwent the combined erosional effects of karstic and glacial processes. For example, large areas of the former Mount Orjen ice-caps (Montenegro) (Hughes et al., 2010) now exhibit a very smooth morphology which is much more typical of karst erosion than glacial erosion. Similarly,

in the Northern Calcareous Alps (Austria), smooth karstic landforms of the Hochschwab plateau are preserved on top of deeply incised glacial valleys. Overall, we note that the morphology of our studied site bears strong similarities with the western flank of the Crvanj mountains (Bosnia and Herzegovina), which is topped by a gently dipping karstic plateau analogous to the Mnaitra plateau, and covered by, presumably LGM, glacial moraines at its base (Žebre et al., 2019). In addition, our reconstruction of the paleo-glaciers involves the Sawda valley glacial tongue, which extended over a very gently sloping (less than  $1^\circ$ ) trough between about 2950 and 2800 m a.s.l. This glacial tongue was irregularly connected to the ice mass that built the Manhale moraine through a dramatically thinned section of ice cascading on the flank of the Cedars cirque (Fig. 6a). In that context, we think that the glacial tongue of the Sawda valley essentially behaved as a plateau glacier, often not associated with the sharp morphologies typical of glacial valleys (i.e. trimlines).

The uncertainties associated with the exposure ages obtained from the Bayesian inversion of the  $^{36}\text{Cl}$  Manhale depth-profile correspond to the  $2\sigma$  Bayesian uncertainty calculated from the sampling distribution of the Markov chain, and thus include the uncertainties associated with both the  $^{36}\text{Cl}$  measurements and the  $^{36}\text{Cl}$  production rate. The major additional source of uncertainty arises from the choice of the model bulk density. Propagation of uncertainties associated with our density estimate into age uncertainties can be assessed from Table 2. According to field observations and measurements, we consider that the  $1.6\text{--}1.8\text{ g cm}^{-3}$  interval, for which the Bayesian inversion yielded exposure-ages ranging from  $25.4 \pm 3.1$  ka to  $31.2 \pm 4.5$  ka (Table 2), represents a conservative interval. The use of the depth profile for those type of morainic deposits avoids problems related to erosion and weathering being especially difficult to account for in the age estimates when sampling solely surface samples (e.g. Žebre et al., 2019). These results place the maximum advance of the Manhale glacier near the upper limit of the global LGM (26.5–19.0ka in Clark et al. (2009) and 27.5–23.4 ka in Hughes and Gibbard (2015)). The LGM paleo-glaciers identified in the present study represent the first evidence of LGM glaciers in the SE Mediterranean following initial suggestion by Messerli (1966) (Fig. 1a). The early timing of maximum glacier extension in this part of the Mediterranean appears consistent with results obtained from the closest glacial deposits preserved in climatically similar environments, i.e. in the Taurus range of Turkey, and farther in Greece on the topographic highs of the Pindus Mountains and Peloponnese. In these mountains, LGM glaciers generally advanced and stabilized before or in the early phase of the global LGM: at about 30 ka on the Dedegöl Mountains (Köse et al., 2019), at 35–28 ka on Mt Akdag (Sarıkaya and Çiner, 2015), at 29–26 ka on Mt Tymphi (Allard et al., 2020), and at 27–23 ka on Mt Chelmos (Pope et al., 2017).

In addition, the ELA reconstruction of the Mount Lebanon glaciers (~2400 m) compares well with values obtained for the above-cited regions: between 2000 and 2700 m in Turkey with most LGM ELAs clustering around 2300–2500 m (see the compilation of Sarıkaya and Ciner, 2015), and between 2000 and 2100 m in Greece (Allard et al., 2020; Pope et al., 2017). More generally, it is consistent with a LGM drop of the ELA to about 2400 m in the transitional zone between the northern temperate climate and the sub-tropical deserts in the eastern Mediterranean (between  $34^\circ\text{N}$  and  $36^\circ\text{N}$ ), as suggested by the interpolation of Mediterranean data (Fig. 1a). ELA contours of the Levant region in Fig. 1a were drawn from the map of Messerli (1966), itself based on moraines identified at 2500 m by the author. Therefore, the lower ELA suggested by our results is simply a consequence of the slightly lower elevation of the moraines reported in the present study. It thus suggests that the moraines of Messerli (1966) might either be associated with slightly

less extensive (younger?) development of glaciers, or reflect slightly different local conditions.

We stress that, to a first order, the widespread absence of LGM glaciers in the SE Mediterranean reflects the absence of high topography (Fig. 1a). In that sense, the presence of past glaciers in Lebanon appears directly related to the structural transpressive bend along the Dead-Sea transform plate boundary (Fig. 1a), across which Mount Lebanon has been uplifted over the last few million years (Elias et al., 2007).

## 5.2. Local and regional paleoclimatic implications

The ELA interval constrained from the reconstruction of the Mount Lebanon LGM glaciers has been converted into a solution space of cooling ( $\Delta T$ ) and factor of precipitation change (FP) using a degree-day model (Brugger, 2006; Hughes and Braithwaite, 2008) (section 4 and Fig. 6b). The thick black line in Fig. 6b corresponds to our preferred estimate, which is based on a 2400-m-ELA, a 100-mm-increase correction of the annual precipitation from the climatic station of Bcharre to the area of the paleo-glaciers (based on the precipitation map of Fig. 2a), and a degree-day factor of 4.1 mm/day/ $^{\circ}$ C. The dark gray envelope encompasses the conservative estimates, which allow the LGM ELA to range between 2310 and 2650 m, and the annual precipitation correction to reach up to 150 mm. As commonly observed in such ( $\Delta T$ ; FP) plots, the ELA is very sensitive to changes in temperature, but much less to changes in precipitation (Fig. 6b). For unchanged precipitation relative to the present, the ELA interval constrained for the Mount Lebanon glaciers would indicate a cooling of  $\sim 7$ – $8$   $^{\circ}$ C relative to modern conditions (Fig. 6b). One the other hand, the ( $\Delta T$ ; FP) solution demonstrates that the reconstructed glaciers would allow a maximum cooling of 10–11  $^{\circ}$ C, a value obtained by considering extremely dry, probably unrealistic, conditions (i.e. factor of precipitation change reduced to 0.1) (Fig. 6b). We recall that the possibility of excess snow brought by the dominant winds blowing from the West, would imply that any reconstructed precipitation represents a maximum precipitation (see section 5.1).

The major uncertainty associated with the LGM climate in the Levant region resides in the hydrological regime: was the LGM climate dry or wet relative to the present? To address this question, we summarize LGM cooling estimates in the Levant, and incorporate them into the ( $\Delta T$ ; FP) plot of Fig. 6b to bracket possible values of FP. The considered paleo-temperature records are of four types: alkenone-derived Sea Surface Temperature offshore Israel (Almogi-Labin et al., 2009; Essallami et al., 2007), a pollen sequence in the Ghab valley, northwest Syria (Wu et al., 2007),  $\delta D$  values of speleothem fluid inclusions in the Peqiin cave, northern Israel, and in the Soreq cave, Central Israel (McGarry et al., 2004), and clumped-isotope thermometry on speleothem carbonates in the Soreq cave (Affek et al., 2008). The LGM cooling determined by these studies range between 6  $^{\circ}$ C and 14  $^{\circ}$ C (in good agreement with our estimate of 10–11  $^{\circ}$ C at most) and are reported in Fig. 6b. It has to be noticed that these paleo-temperature records cover different periods of the LGM from 18.6 to 29.0 ka (color-coded as “Late LGM” or “LGM” in Fig. 6b).

Each of the paleo-temperature estimates has been converted into a factor of precipitation change according to the space of ( $\Delta T$ ; FP) solutions constrained by our glacial reconstruction (double arrows in Fig. 6b). The results show that all the continental paleo-temperature records older than 20 ka invariably require a decrease in the rate of precipitation when considering the classical value of 4.1 mm/day/ $^{\circ}$ C for the degree-day factor (orange arrows in Fig. 6b). We still note that the reconstructed glacier extent might be compatible with a slight increase in precipitation under the condition that the degree-day factor approaches the extreme bound of

its conservative interval, that is close to 5.6 mm/day/ $^{\circ}$ C. This possibility is very unlikely however given the distribution of degree-day factors derived from direct observations (Braithwaite, 2008). Although  $^{36}$ Cl dating indicates that the Manhale glacier reached its maximum advance prior to 20 ka, we have derived FP values using Late LGM paleo-temperature records (yellow arrows in Fig. 6b) for comparison. It shows that these late terrestrial records would be compatible with a wide range of FP, because the slightly lower cooling reported for that time interval project onto the steeper (left-hand side) section of the ( $\Delta T$ ,FP) plot, where the ELA varies very little as a function of precipitation rates (Fig. 6b). For the same reason, the marine records, which span the 19.0–24.0 ka interval, would imply either a decrease (Almogi-Labin et al., 2009) or an increase (Essallami et al., 2007) in the rate of precipitation. Given both the Early LGM age of the Manhale moraine and its terrestrial location, the cooling of 8–11  $^{\circ}$ C at Peqiin cave (McGarry et al., 2004), of 8–14  $^{\circ}$ C in the Ghab valley (Wu et al., 2007), and of 9–14  $^{\circ}$ C at Soreq cave (McGarry et al., 2004) appear as the most appropriate paleo-temperature records to derive paleo-precipitation estimates from the reconstructed ELA (orange arrows in Fig. 6b). These records suggest that the local climate must have been drier than the modern conditions to restrict the Mount Lebanon glaciers to their reconstructed extents.

Moreover, it should be noted that the LGM cooling values used in Fig. 6b are constrained from sites lying at least 1500 m below the Mount Lebanon paleo-glaciers. Therefore, if the LGM lapse-rate in the Mediterranean was steeper than 6.5  $^{\circ}$ C/km as suggested by Kuhlemann et al. (2008), then the cooling values used in Fig. 6b would underestimate the LGM cooling at our studied site. This would in turn enhance the precipitation reduction implied by the ( $\Delta T$ ,FP) plot. The same shift towards even drier conditions would be obtained if the reconstructed glaciers were partly built from wind-blown snow as discussed in section 5.1. A dry LGM over Mount Lebanon is consistent with the oxygen isotope record of ostracod shells in the Yammouneh paleo-lake, located as close as 12 km from our studied site. This indicates that the LGM was a period of local water deficit (Develle et al., 2011). Similarly, dry conditions appear to characterize the last four glacial stages at the same site (Gasse et al., 2015). The Jeita cave isotope record (from the Lebanon coast) (Cheng et al., 2015) follows the same trend during LGM as the speleothem records further south (Central and South Israel) (Bar-Matthews et al., 2019). However, the slow deposition of the Jeita cave speleothem during the glacial period as well as the consideration of the source effect from the Mediterranean Sea on the isotope record support less wet conditions during most of last glacial in the region (Bar-Matthews et al., 2019). LGM lake high-stands in the Lisan-Dead Sea Basin, some 150 km further S in Israel (Fig. 1b), have long been attributed to regionally increased precipitation (Stein et al., 2010; Torfstein et al., 2013a, 2013b). A recent study by Miebach et al. (2019) conducted on pollens from Lake Lisan sediments provides evidence that the glacial pollen record was not necessarily associated with precipitation increase during LGM. This is in line with a modeling study suggesting the glacial high-stands in Lake Lisan were best explained by a decrease in evaporation that compensated the concomitant decrease in the rates of precipitation (Stockhecke et al., 2016).

On a broader geographical scale, long-term transient simulations from a coupled atmosphere-ocean-sea-ice-vegetation model (LOVECLIM) show that the northern hemisphere ice sheets during glacial stages had a strong impact on atmospheric circulation causing a massive drying in the eastern Mediterranean and in the Levant (Stockhecke et al., 2016). As shown by a LGM simulation from a general circulation model (PMIP-2), the mid-latitude westerly belt was pushed southward in response to the ice sheet and sea ice extent at northern high latitudes (Lainé et al., 2009).

## 6. Conclusions

We have identified morphological and sedimentological evidence that testify to the existence of past glaciers on the western side of Mount Lebanon. The maximum advance of three glaciers (one 8-km-long glacial tongue and two small glacier cirques) has been inferred from their geometries. The deposition of the largest glacier frontal moraine has been dated to  $25.4 \pm 3.1$ – $31.2 \pm 4.5$  ka based on  $^{36}\text{Cl}$  Cosmic Ray Exposure dating of a 10 m deep profile in the constitutive diamicton. The reconstructed glacier hypsometry indicates that this maximum glacier extension occurred along an Equilibrium Line Altitude depressed to about 2400 m using the AAR method. The early LGM age obtained for the maximum glacier advance matches with glacial chronologies obtained from other Eastern Mediterranean moraines (in particular in Turkey and Greece). Finally, a degree-day model was used to infer the LGM paleo-climatic conditions required to depress the ELA to about 2400 m. It suggests that, under the LGM cooling conditions documented for the Levant region, the local climate was drier compared to modern conditions. This study highlights the complexity of Mediterranean climatic responses, in an area influenced by several factors (large scale climate pattern, local orography, active tectonics). Inputs of several climate archives, although influenced by different biases, provide clues to answer the questions of spatial heterogeneities of the palaeohydrological response in the Levant.

In the Mediterranean region it is therefore crucial to combine all approaches to reconstructing climate change in order to resolve fine-scale variations and to validate certain paleoclimatic proxies.

## Credit author statement

The authors had the following roles during the realization of this study: initiation of the project (Tapponnier, Benedetti, Daeron, Elias, Vidal), field work and mapping (Moulin, Benedetti, Van der Woerd, Hage-Hassan, Elias, Daeron), sample preparation (Moulin, Hage-Hassan), data analysis (Moulin, Benedetti, Schimmelpennig), paleo-climatic interpretation (Moulin, Vidal), writing (Moulin, Benedetti, Vidal, Elias, Schimmelpennig).

## Declaration of competing interest

The authors declare that they have no known competing financial interests or personal relationships that could have appeared to influence the work reported in this paper.

## Acknowledgements

The French CNRS-INSU-LEFE-EVE (PaleoLIBAN) programme provided financial support for field work and sample analysis (LV). Jenna Hage-Hassan's scientific visit at CEREGE was supported by Labex OT-Med (ANR-11-LABX-0061). Anne-Lise Develle participated in one of the first field trip and is acknowledged for support and help in the field. We warmly acknowledge A. Sursok (CNRG, Lebanon), and all his team, for help and support in the field.

## Appendix A. Supplementary data

Supplementary data to this article can be found online at <https://doi.org/10.1016/j.quascirev.2022.107502>.

## References

- Abi-Saleh, B., Safi, S., 1988. Carte de la végétation du Liban. *Ecol. Mediterr.* 14 (1), 123–141.
- Affek, H.P., Bar-Matthews, M., Ayalon, A., Matthews, A., Eiler, J.M., 2008. Glacial/interglacial temperature variations in Soreq cave speleothems as recorded by 'clumped isotope' thermometry. *Geochem. Cosmochim. Acta* 72 (22), 5351–5360.
- Allard, J.L., Hughes, P.D., Woodward, J.C., Fink, D., Simon, K., Wilcken, K.M., 2020. Late Pleistocene glaciers in Greece: a new  $^{36}\text{Cl}$  chronology. *Quat. Sci. Rev.* 245, 106528.
- Allard, James L., Hughes, Philip D., Woodward, Jamie C., 2021. A radiometric dating revolution and the Quaternary glacial history of the Mediterranean mountains. *Earth Sci. Rev.* 223, 103844.
- Allen, R., Siegert, M.J., Payne, A.J., 2008. Reconstructing glacier-based climates of LGM Europe and Russia—Part 2: a dataset of LGM precipitation/temperature relations derived from degree-day modelling of palaeo glaciers. *Clim. Past* 4 (4), 249–263.
- Almogi-Labin, A., Bar-Matthews, M., Shriki, D., Kolosovsky, E., Paterne, M., Schilman, B., et al., 2009. Climatic variability during the last-90 ka of the southern and northern Levantine Basin as evident from marine records and speleothems. *Quat. Sci. Rev.* 28 (25–26), 2882–2896.
- Anderson, S.P., 1988. The upfreezing process: experiments with a single clast. *Geol. Soc. Am. Bull.* 100 (4), 609–621.
- Balco, G., 2017. Production rate calculations for cosmic-ray-muon-produced  $^{10}\text{Be}$  and  $^{26}\text{Al}$  benchmarked against geological calibration data. *Quat. Geochronol.* 39, 150–173.
- Bar-Matthews, M., Keinan, J., Ayalon, A., 2019. Hydro-climate research of the late Quaternary of the Eastern Mediterranean-Levant region based on speleothems research—A review. *Quat. Sci. Rev.* 221, 105872.
- Barry, R.G., Chorley, R.J., 2009. *Atmosphere, Weather and Climate*. Routledge.
- Bennett, M.R., Boulton, G.S., 1993. A reinterpretation of scottish 'hummocky moraine' and its significance for the deglaciation of the scottish highlands during the younger dryas or loch lomond stadial. *Geol. Mag.* 130 (3), 301–318.
- Bennett, M.R., 1994. Morphological evidence as a guide to deglaciation following the Loch Lomond Readvance: a review of research approaches and models. *Scot. Geogr. Mag.* 110 (1), 24–32.
- Blard, P.H., Lavé, J., Farley, K.A., Fornari, M., Jiménez, N., Ramirez, V., 2009. Late local glacial maximum in the Central Altiplano triggered by cold and locally-wet conditions during the paleolake Tauca episode (17–15 ka, Heinrich 1). *Quat. Sci. Rev.* 28 (27–28), 3414–3427.
- Boone, S.J., Eyles, N., 2001. Geotechnical model for great plains hummocky moraine formed by till deformation below stagnant ice. *Geomorphology* 38 (1–2), 109–124.
- Braithwaite, R.J., 2008. Temperature and precipitation climate at the equilibrium-line altitude of glaciers expressed by the degree-day factor for melting snow. *J. Glaciol.* 54 (186), 437–444.
- Braithwaite, R.J., Raper, S.C., Chutko, K., 2006. Accumulation at the equilibrium-line altitude of glaciers inferred from a degree-day model and tested against field observations. *Ann. Glaciol.* 43, 329–334.
- Braithwaite, R.J., Zhang, Y., 2000. Sensitivity of mass balance of five Swiss glaciers to temperature changes assessed by tuning a degree-day model. *J. Glaciol.* 46 (152), 7–14.
- Braithwaite, R.J., 1984. Calculation of degree-days for glacier-climate research. *Z. Gletscherkd. Glazialgeol.* 20 (1984), 1–8.
- Braithwaite, R.J., Olesen, O.B., 1989. Calculation of glacier ablation from air temperature, West Greenland. In: *Glacier Fluctuations and Climatic Change*. Springer, Dordrecht, pp. 219–233.
- Braithwaite, R.J., Raper, S.C., 2007. Glaciological conditions in seven contrasting regions estimated with the degree-day model. *Ann. Glaciol.* 46, 297–302.
- Braucher, R., Del Castillo, P., Sime, L., Hidy, A.J., Bourles, D.L., 2009. Determination of both exposure time and denudation rate from an in situ-produced  $^{10}\text{Be}$  depth profile: a mathematical proof of uniqueness. Model sensitivity and applications to natural cases. *Quat. Geochronol.* 4 (1), 56–67.
- Brugger, K.A., 2006. Late Pleistocene climate inferred from the reconstruction of the Taylor River glacier complex, southern Sawatch Range, Colorado. *Geomorphology* 75 (3–4), 318–329.
- Cheddadi, R., Khater, C., 2016. Climate change since the last glacial period in Lebanon and the persistence of Mediterranean species. *Quat. Sci. Rev.* 150, 146–157.
- Cheng, H., Sinha, A., Verheyden, S., Nader, F.H., Li, X.L., Zhang, P.Z., et al., 2015. The climate variability in northern Levant over the past 20,000 years. *Geophys. Res. Lett.* 42 (20), 8641–8650.
- Çiner, A., Stepišnik, U., Sarikaya, M.A., Žebre, M., Yildirim, C., 2019. Last glacial maximum and younger dryas piedmont glaciations in blidinje, the dinaric mountains (Bosnia and Herzegovina): insights from  $^{36}\text{Cl}$  cosmogenic dating. *Mediterranean Geoscience Reviews* 1 (1), 25–43.
- Clark, P.U., Dyke, A.S., Shakun, J.D., Carlson, A.E., Clark, J., Wohlfarth, B., et al., 2009. The last glacial maximum. *Science* 325 (5941), 710–714.

- Daéron, M., Klinger, Y., Tapponnier, P., Elias, A., Jacques, E., Surssock, A., 2007. 12,000-year-long record of 10 to 13 paleoearthquakes on the Yammouneh fault, Levant fault system, Lebanon. *Bull. Seismol. Soc. Am.* 97 (3), 749–771.
- Dahl, S.O., Nesje, A., 1992. Paleoclimatic implications based on equilibrium-line altitude depressions of reconstructed Younger Dryas and Holocene cirque glaciers in inner Nordfjord, western Norway. *Palaeogeogr. Palaeoclimatol. Palaeoecol.* 94 (1–4), 87–97.
- Develle, A.L., Gasse, F., Vidal, L., Williamson, D., Demory, F., Van Campo, E., et al., 2011. A 250 ka sedimentary record from a small karstic lake in the Northern Levant (Yammoûneh, Lebanon): paleoclimatic implications. *Palaeogeogr. Palaeoclimatol. Palaeoecol.* 305 (1–4), 10–27.
- Dubertret, L., 1955. Note explicative de la carte géologique du Liban au 1/200 000 Beirut. *Muséum national d'histoire naturelle*.
- Ehlers, J., Gibbard, P.L., 2004. Quaternary Glaciations-Extent and Chronology: Part I: Europe. Elsevier.
- Elias, A., Tapponnier, P., Singh, S.C., King, G.C., Briais, A., Daéron, M., et al., 2007. Active thrusting offshore Mount Lebanon: source of the tsunamigenic AD 551 Beirut-Tripoli earthquake. *Geology* 35 (8), 755–758.
- Emeis, K.C., Schulz, H., Struck, U., Rossignol-Strick, M., Erlenkeuser, H., Howell, M.W., et al., 2003. Eastern Mediterranean surface water temperatures and  $\delta^{18}O$  composition during deposition of sapropels in the late Quaternary. *Paleoceanography* 18 (1).
- Essallami, L., Sicre, M.A., Kallel, N., Labeyrie, L., Siani, G., 2007. Hydrological changes in the Mediterranean Sea over the last 30,000 years. *Geochem. Geophys. Geosyst.* 8 (7).
- Farinotti, D., Immerzeel, W.W., de Kok, R.J., Quincey, D.J., Dehecq, A., 2020. Manifestations and mechanisms of the karakoram glacier anomaly. *Nat. Geosci.* 13 (1), 8–16.
- Fifield, L.K., Ophel, T.R., Allan, G.L., Bird, J.R., Davie, R.F., 1990. Accelerator mass spectrometry at the Australian National University's 14UD accelerator: experience and developments. *Nucl. Instrum. Methods Phys. Res. Sect. B Beam Interact. Mater. Atoms* 52 (3–4), 233–237.
- Ford, D., Williams, P.D., 2013. *Karst Hydrogeology and Geomorphology*. John Wiley & Sons.
- Gasse, F., Vidal, L., Van Campo, E., Demory, F., Develle, A.L., Tachikawa, K., et al., 2015. Hydroclimatic changes in northern Levant over the past 400,000 years. *Quat. Sci. Rev.* 111, 1–8.
- Goodman, J., Weare, J., 2010. Ensemble samplers with affine invariance. *Commun. Appl. Math. Comput. Sci.* 5 (1), 65–80.
- Gvirtzman, G., Wieder, M., 2001. Climate of the last 53,000 years in the eastern Mediterranean, based on soil-sequence stratigraphy in the coastal plain of Israel. *Quat. Sci. Rev.* 20 (18), 1827–1849.
- Hajar, L., Haïdar-Boustani, M., Khater, C., Cheddadi, R., 2010. Environmental changes in Lebanon during the Holocene: man vs. climate impacts. *J. Arid Environ.* 74 (7), 746–755.
- Heisinger, B., Lal, D., Jull, A.J.T., Kubik, P., Ivy-Ochs, S., Neumaier, S., et al., 2002a. Production of selected cosmogenic radionuclides by muons: 1. Fast muons. *Earth Planet Sci. Lett.* 200 (3–4), 345–355.
- Heisinger, B., Lal, D., Jull, A.J.T., Kubik, P., Ivy-Ochs, S., Knie, K., Nolte, E., 2002b. Production of selected cosmogenic radionuclides by muons: 2. Capture of negative muons. *Earth Planet Sci. Lett.* 200 (3–4), 357–369.
- Hewitt, G.M., 2004. Genetic consequences of climatic oscillations in the Quaternary. *Phil. Trans. Roy. Soc. Lond. B Biol. Sci.* 359 (1442), 183–195.
- Hewitt, K., 2011. Glacier change, concentration, and elevation effects in the karakoram himalaya, upper indus basin. *Mt. Res. Dev.* 31 (3), 188–200.
- Hidy, A.J., Gosse, J.C., Pederson, J.L., Mattern, J.P., Finkel, R.C., 2010. A geologically constrained Monte Carlo approach to modeling exposure ages from profiles of cosmogenic nuclides: an example from Lees Ferry, Arizona. *Geochem. Geophys. Geosyst.* 11 (9).
- Hodgson, D., 1982. Hummocky and Fluted Moraines in Part of North-West Scotland. Hughes, P.D., Woodward, J., Gibbard, P.L., 2006. Late Pleistocene glaciers and climate in the mediterranean. *Global Planet. Change* 50 (1–2), 83–98.
- Hughes, P.D., Braithwaite, R.J., 2008. Application of a degree-day model to reconstruct Pleistocene glacial climates. *Quat. Res.* 69 (1), 110–116.
- Hughes, P.D., Woodward, J.C., Van Calsteren, P.C., Thomas, L.E., Adamson, K.R., 2010. Pleistocene ice caps on the coastal mountains of the Adriatic Sea. *Quat. Sci. Rev.* 29 (27–28), 3690–3708.
- Hughes, P.D., Gibbard, P.L., 2015. A stratigraphical basis for the last glacial maximum (LGM). *Quat. Int.* 383, 174–185.
- Hughes, P.D., Woodward, J.C., 2017. Quaternary glaciation in the Mediterranean mountains: a new synthesis. *Geol. Soc. Lond. Special Public.* 433 (1), 1–23.
- Hughes, P.D., Fink, D., Fletcher, W., 2020. Late Pleistocene glaciers and climate in the high Atlas, North Africa. *Untangling Quat. Period: A Legacy of Stephen C. Porter* (eds Waitt, R.B., Thackray, G.D. & Gillespie, A.R.). *Geol. Soc. Amer. Spec. Pap.* 10 (2020), 8, 2548.
- Jomelli, V., Favier, V., Rabatel, A., Brunstein, D., Hoffmann, G., Francou, B., 2009. Fluctuations of glaciers in the tropical Andes over the last millennium and palaeoclimatic implications: a review. *Palaeogeogr. Palaeoclimatol. Palaeoecol.* 281 (3–4), 269–282.
- Kuhlemann, J., Rohling, E.J., Krumrei, I., Kubik, P., Ivy-Ochs, S., Kucera, M., 2008. Regional synthesis of mediterranean atmospheric circulation during the last glacial maximum. *Science* 321 (5894), 1338–1340.
- Kern, Z., László, P., 2010. Size specific steady-state accumulation-area ratio: an improvement for equilibrium-line estimation of small paleoglaciologists. *Quat. Sci. Rev.* 29 (19–20), 2781–2787.
- Köse, O., Sarikaya, M.A., Çiner, A., Candaş, A., 2019. Late Quaternary glaciations and cosmogenic  $^{36}Cl$  geochronology of Mount Dedegöl, south-west Turkey. *J. Quat. Sci.* 34 (1), 51–63.
- Lañé, A., Kageyama, M., Salas-Méla, D., Voltaire, A., Riviere, G., Ramstein, G., et al., 2009. Northern hemisphere storm tracks during the last glacial maximum in the PMIP2 ocean-atmosphere coupled models: energetic study, seasonal cycle, precipitation. *Clim. Dynam.* 32 (5), 593–614.
- Lal, D., 1991. Cosmic ray labeling of erosion surfaces: in situ nuclide production rates and erosion models. *Earth Planet Sci. Lett.* 104 (2–4), 424–439.
- Maheras, P., 1988. Les types de temps synoptiques au-dessus de la Méditerranée Orientale. *Méditerranée* 66 (4), 35–42.
- McGarry, S., Bar-Matthews, M., Matthews, A., Vaks, A., Schilman, B., Ayalon, A., 2004. Constraints on hydrological and paleotemperature variations in the Eastern Mediterranean region in the last 140 ka given by the  $\delta D$  values of speleothem fluid inclusions. *Quat. Sci. Rev.* 23 (7–8), 919–934.
- Médail, F., Diadema, K., 2009. Glacial refugia influence plant diversity patterns in the Mediterranean Basin. *J. Biogeogr.* 36 (7), 1333–1345.
- Messerli, B., 1966. Das problem der eiszeitlichen Vergletscherung am Libanon und Hermon. *Borntraeger*.
- Miebach, A., Stolzenberger, S., Wacker, L., Hense, A., Litt, T., 2019. A new Dead Sea pollen record reveals the last glacial paleoenvironment of the southern Levant. *Quat. Sci. Rev.* 214, 98–116.
- Mikolajewicz, U., 2011. Modeling mediterranean ocean climate of the last glacial maximum. *Clim. Past* 7, 161–180.
- Mix, A.C., Bard, E., Schneider, R., 2001. Environmental processes of the ice age: land, oceans, glaciers (EPILOG). *Quat. Sci. Rev.* 20 (4), 627–657.
- Oerlemans, J., 2005. Extracting a climate signal from 169 glacier records. *Science* 308 (5722), 675–677.
- Pellitero, R., Rea, B.R., Spagnolo, M., Bakke, J., Ivy-Ochs, S., Frew, C.R., et al., 2016. GlaRe, a GIS tool to reconstruct the 3D surface of paleoglaciologists. *Comput. Geosci.* 94, 77–85.
- Pellitero, R., Rea, B.R., Spagnolo, M., Bakke, J., Hughes, P., Ivy-Ochs, S., et al., 2015. A GIS tool for automatic calculation of glacier equilibrium-line altitudes. *Comput. Geosci.* 82, 55–62.
- Petit, R.J., Aguinagalde, I., de Beaulieu, J.L., Bittkau, C., Brewer, S., Cheddadi, R., et al., 2003. Glacial refugia: hotspots but not melting pots of genetic diversity. *Science* 300 (5625), 1563–1565.
- Plassard, J., 1981. *Atlas climatique du Liban. Ministère des travaux publics et des transports, service météorologique du Liban, vol. 1. observatoire de Ksara, Beyrouth.*
- Pope, R.J., Hughes, P.D., Skourtso, E., 2017. Glacial history of Mt Chelmos, peloponnesus, Greece. *Geol. Soc. Lond. Special Public.* 433 (1), 211–236.
- Porter, S.C., 2000. Snowline depression in the tropics during the last glaciation. *Quat. Sci. Rev.* 20 (10), 1067–1091.
- Protin, M., Schimmelpfennig, I., Mugnier, J.L., Ravel, L., Le Roy, M., Deline, P., et al., 2019. Climatic reconstruction for the younger dryas/early holocene transition and the little ice age based on paleo-extents of argentièrè glacier (French Alps). *Quat. Sci. Rev.* 221, 105863.
- Rabatel, A., Francou, B., Jomelli, V., Naveau, P., Grancher, D., 2008. A chronology of the Little Ice Age in the tropical Andes of Bolivia (16 S) and its implications for climate reconstruction. *Quat. Res.* 70 (2), 198–212.
- Refsnider, K.A., Laabs, B.J., Plummer, M.A., Mickelson, D.M., Singer, B.S., Caffee, M.W., 2008. Last glacial maximum climate inferences from cosmogenic dating and glacier modeling of the western Uinta ice field, Uinta Mountains, Utah. *Quat. Res.* 69 (1), 130–144.
- Sanlaville, P., 1977. *Etude géomorphologique de la région littorale du Liban*. Ph.D. Beirut Lebanese University 859 p.
- Sarikaya, M.A., Çiner, A., 2015. Late Pleistocene glaciations and paleoclimate of Turkey. *Maden Tetkik ve Arama Dergisi* 151 (151), 107–127.
- Sankaya, M.A., Zreda, M., Çiner, A., 2009. Glaciations and paleoclimate of Mount Erciyes, central Turkey, since the Last Glacial Maximum, inferred from  $^{36}Cl$  cosmogenic dating and glacier modeling. *Quat. Sci. Rev.* 28 (23–24), 2326–2341.
- Schimmelpfennig, I., Tesson, J., Blard, P.H., Benedetti, L., Zakari, M., Balco, G., 2019. The CREP Chlorine-36 exposure age and depth profile calculator. *Goldschmidt. Schimmelpfennig, I., 2009. Cosmogenic  $^{36}Cl$  in Ca and K Rich Minerals: Analytical Developments, Production Rate Calibrations and Cross Calibration with  $^{3}He$  and  $^{21}Ne$  (Doctoral dissertation, Aix-Marseille 3).*
- Schlagenhauf, A., Manighetti, L., Benedetti, L., Gaudemer, Y., Finkel, R., Malavieille, J., Pou, K., 2011. Earthquake supercycles in Central Italy, inferred from  $^{36}Cl$  exposure dating. *Earth Planet Sci. Lett.* 307 (3–4), 487–500.
- Sharma, P., Kubik, P.W., Fehn, U., Gove, H.E., Nishiizumi, K., Elmore, D., 1990. Development of  $^{36}Cl$  standards for AMS. *Nucl. Instrum. Methods Phys. Res. Sect. B Beam Interact. Mater. Atoms* 52 (3–4), 410–415.
- Stein, M., Torfstein, A., Gavrieli, I., Yechieli, Y., 2010. Abrupt aridities and salt deposition in the post-glacial Dead Sea and their North Atlantic connection. *Quat. Sci. Rev.* 29 (3–4), 567–575.
- Stockhecke, M., Timmermann, A., Kipfer, R., Haug, G.H., Kwiczen, O., Friedrich, T., et al., 2016. Millennial to orbital-scale variations of drought intensity in the Eastern Mediterranean. *Quat. Sci. Rev.* 133, 77–95.
- Stone, J.O., 2000. Air pressure and cosmogenic isotope production. *J. Geophys. Res. Solid Earth* 105 (B10), 23753–23759.
- Stone, J., Evans, J., Fifield, K., Cresswell, R., Allan, G., 1996. Cosmogenic chlorine-36 production rates from calcium and potassium. *Radiocarbon* 38 (1), 170–171.
- Styllas, M.N., Schimmelpfennig, I., Benedetti, L., Ghilardi, M., Aumaitre, G.,

- Bourlès, D., Keddadouche, K., 2018. Late-glacial and Holocene history of the northeast Mediterranean mountain glaciers-New insights from in situ-produced  $^{36}\text{Cl}$ -based cosmic ray exposure dating of paleo-glacier deposits on Mount Olympus, Greece. *Quat. Sci. Rev.* 193, 244–265.
- Torfstein, A., Goldstein, S.L., Kagan, E.J., Stein, M., 2013a. Integrated multi-site U–Th chronology of the last glacial Lake Lisan. *Geochem. Cosmochim. Acta* 104, 210–231.
- Torfstein, A., Goldstein, S.L., Stein, M., Enzel, Y., 2013b. Impacts of abrupt climate changes in the levant from last glacial Dead Sea levels. *Quat. Sci. Rev.* 69, 1–7.
- Walley, C.D., 1997. The lithostratigraphy of Lebanon: a review. *Lebanese Sci. Bull.* 10 (1), 81–108.
- Wu, H., Guiot, J., Brewer, S., Guo, Z., 2007. Climatic changes in Eurasia and Africa at the last glacial maximum and mid-Holocene: reconstruction from pollen data using inverse vegetation modelling. *Clim. Dynam.* 29 (2–3), 211–229.
- Žebre, M., Sarikaya, M.A., Stepišnik, U., Yıldırım, C., Çiner, A., 2019. First  $^{36}\text{Cl}$  cosmogenic moraine geochronology of the Dinaric mountain karst: velež and Crvanj Mountains of Bosnia and Herzegovina. *Quat. Sci. Rev.* 208, 54–75.